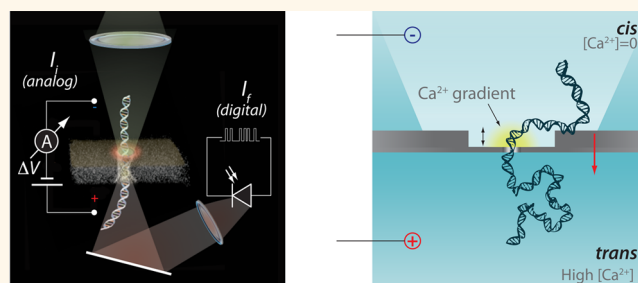


Probing Solid-State Nanopores with Light for the Detection of Unlabeled Analytes

Brett N. Anderson,[†] Ossama N. Assad,[‡] Tal Gilboa,[‡] Allison H. Squires,[†] Daniel Bar,[‡] and Amit Meller^{*,†,‡}

[†]Department of Biomedical Engineering Boston University Boston, Massachusetts 02215, United States and [‡]Department of Biomedical Engineering The Technion - Israel Institute of Technology Haifa, Israel 32000

ABSTRACT Nanopore sensing has enabled label-free single-molecule measurements on a wide variety of analytes, including DNA, RNA, and protein complexes. Much progress has been made toward biotechnological applications; however, electrically probing the ion current introduces nonideal noise components. Here we further develop a method to couple an ionic current to a photon-by-photon counting of fluorescent signal from Ca^{2+} -sensitive dyes and demonstrate label-free optical detection of biopolymer translocation through solid-state nanopores using TIRF and confocal microscopy.



We show that by fine adjustment of the CaCl_2 gradient, EGTA concentration, and voltage, the optical signals can be localized to the immediate vicinity of the pore. Consequently, the noise spectral density distribution in the optical signal exhibits a nearly flat distribution throughout the entire frequency range. With the use of high-speed photon counting devices in confocal microscopy and higher photon count rates using stronger light sources, we can improve the signal-to-noise ratio of signal acquisition, while the use of wide-field imaging in TIRF can allow for simultaneous quantitative imaging of large arrays of nanopores.

KEYWORDS: solid-state nanopores · optical sensing · total internal reflection fluorescence · confocal microscopy · photon counting

Nanopores are electrophoretic single-molecule sensors composed of an ultrathin insulating membrane (typically a few nanometers thick) separating two liquid chambers in which a nanoscale pore is formed. Nanopore sensing^{1,2} utilizes electrical measurement of the ion current through the pore as a means to probe the entry and passage of electrically charged biomolecules, such as DNA,^{3,4} RNA,⁵ and proteins.^{6–8} Nanopore measurements are both very general and exquisitely sensitive: When an analyte occupies the nanopore volume, the ionic conductance is modulated, resulting in measurable changes in the ionic current. This principle has been broadly utilized for a variety of sensing applications in biotechnology,⁹ most prominently for direct, single-molecule nucleic acid sequencing,^{10–13} for probing RNA structures,^{14–16} and for genotyping viral genes.¹⁷

In recent years, substantial progress has been made to improve the ability of

nanopores to distinguish fine macromolecular features. Key to these developments have been improved control over analyte translocation speed,^{11,18–22} reduced electrical noise,²³ and increased detection bandwidth.^{8,23} To date, however, purely electrical sensing of solid-state nanopores remains hindered by the color of the ion current noise spectra, which includes lower frequency ($1/f$) flicker noise as well as higher frequency dielectric loss and capacitive noise, on top of the flat thermal noise (Johnson-Nyquist) and electronic shot noise.²³ While the physical origins of the latter noise sources have previously been well characterized,^{23–25} the source of $1/f$ noise, which is present in both biological and solid-state nanopore systems, is not fully understood. Past work has implicated surface charge fluctuations²⁶ or an inverse scaling with the total number of mobile charge carriers (obeying Hooke's phenomenological relation).^{25,27} Eliminating flicker noise is of particular interest in the context

* Address correspondence to ameller@bu.edu.

Received for review September 29, 2014 and accepted November 2, 2014.

Published online November 02, 2014
10.1021/nn505545h

© 2014 American Chemical Society

of nanopore sequencing applications: the most successful approaches have slowed translocation to >1 ms/nt, so correctly determining blockage levels of this duration will be adversely affected by $1/f$ noise, reducing the accuracy of such techniques. Additionally, electrical signals could be further compromised by capacitive crosstalk among neighboring nanopore sensors in arrays consisting of large numbers of nanopores. This poses a challenge for a growing number of future nanopore sensing applications, such as high throughput DNA sequencing or protein detection, which benefit from the ability to simultaneously probe many pores fabricated in a small (micrometer scale) area.

In this paper, we evaluate an alternative nanopore probing method which uses digital photon counting to replace or to complement the electrical measurement. Similar to electrical measurements, this optical sensing technique probes the time-dependent nanopore conductance. However, the optical signals produced in our method are confined to the nanopore and are thus much less subject to noise contamination by other electrical components. Optical signals originating at the nanopore itself are, in principle, free of spurious noise sources, and offer flatter noise spectra and thus a higher potential effective bandwidth given comparable ion and photon count rates. When coupled with low optical noise laser systems for fluorescence excitation and with high-bandwidth single-photon optical sensors (both readily available), a purely digital photon counting method for the ion current detection in nanopores can be realized.

To this end we experimentally and theoretically studied a far-field optical sensing method to detect time-varying ion current intensities, to be used as an alternative or complementary scheme for the electrical measurement of nanopore current. Optical sensing in nanopores is attractive for several reasons: First, the chemical gradients across the nanopore can be fine-tuned to adjust the effective fluorescent spot size around the nanopore, down to nanometer-scale spots. This could enable detection of fine molecular structures by restricting sensing volume in a manner that does not rely upon precise pore geometry. Second, photon noise is characterized by a pure shot noise spectrum ("white noise"), evenly affecting all frequency components of the nanopore signal. Third, far-field optics readily permit detection with massive numbers of nanopores as long as the pore-to-pore separation is on the order of a single wavelength. Fourth, use of multiple excitation/emission colors can be utilized to provide additional information on the probed molecules, significantly enhancing the potential range of applications.

The feasibility of single-molecule optical detection in solid-state nanopores, using fluorescently labeled analytes, such as DNA, has already been

demonstrated.^{28–34} These approaches have proven useful for the development of DNA sequencing methods of modified DNA molecules; however, they require chemical modifications of the bioanalytes to facilitate coupling of fluorescent moieties. The focus of the current paper is optical detection of unlabeled analytes, utilizing light-intensity modulations emitted by Ca^{2+} ion indicator dyes. A similar approach was first used by Heron and co-workers to probe stochastic cyclodextrin on/off binding kinetics to the α hemolysin protein pore,³⁵ albeit at a narrow bandwidth (up to 400 Hz) and a low photon count rate. Biological nanopores in an artificial bilayer are difficult to use for optical measurements because pore insertion is a stochastic event and pores subsequently diffuse around the membrane, requiring tracking and substantially increasing experimental complexity. This work was followed up using solid-state nanopores by Anderson with TIRF microscopy³⁶ and then by Ivankin and co-workers with epifluorescence microscopy for the detection of unlabeled biopolymer translocation at improved frames rates (up to 4.8 kHz).³⁷

Here we developed TIRF/confocal microscopy to observe fluorescent spots on solid-state nanopores, with >4 orders of magnitude higher photon emission (in confocal mode) than previous reports, enabling higher bandwidth acquisition from dense arrays of pores of arbitrary size. Moreover, we employ a photon-by-photon digital counting technique to circumvent sampling errors and offer a flat, white noise spectral density. Limiting the excitation volume to <100 nm above the surface (TIRF) or to a diffraction limited spot in confocal mode prevented photobleaching of dye molecules in the vicinity of the pore prior to measurement and allowed us to circumvent the flow system required in epifluorescence illumination. We explore this system using extensive numerical simulations and demonstrate agreement with experimental results under a variety of experimental conditions. Finally, we demonstrate the feasibility of simultaneous multi-pore single-molecule sensing using Total Internal Reflection Fluorescence (TIRF).

RESULTS

Opto-Electrical Nanopore Sensing Platform. Solid-state nanopores were fabricated in LPCVD-deposited free-standing membranes of silicon nitride (SiN_x) $20 \times 20 \mu\text{m}^2$ in size. These membranes, initially 60 nm thick, were locally thinned using a controlled Reactive Ion Etching (RIE) process applied to $\sim 2 \mu\text{m}$ diameter wells, resulting in 10 nm thick regions (see Figure 1 and Methods). These thinned regions produce lower optical background and allow for easy localization of the pores in our optical microscope. Nanopore chips were mounted in custom flow cells designed for confocal or TIRF microscopy as reported in Soni *et al.*³⁰ A detailed

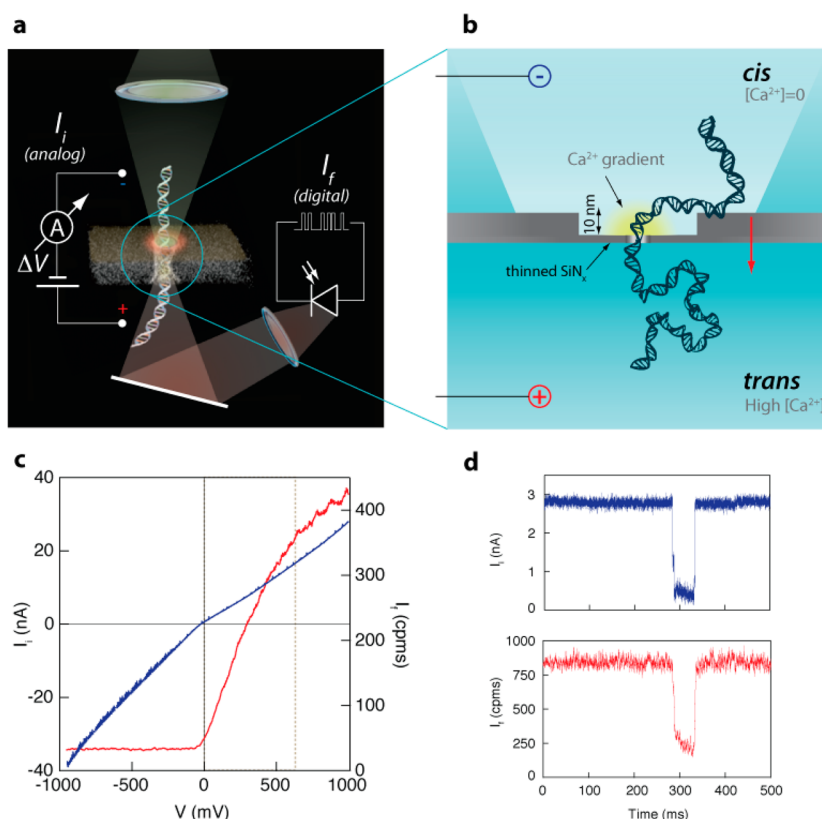


Figure 1. Chemo-optical sensing in solid-state nanopores. (a) The ionic current flowing through a solid-state nanopore is probed both electrically (analog) and optically (digital) in a synchronous manner. For optical probing, a laser spot is focused at the pore region, and emitted light is collected photon-by-photon using an avalanche photo diode. (b) A local and tunable Ca^{2+} ion gradient is created in the vicinity of the pore at the *cis* side, where a low concentration of Ca^{2+} activated fluorophores is present. Entry and transport of DNA molecule through the pore modulate the ion current and hence the fluorescence intensity. (c) Ion current versus voltage curves measured both electrically (blue curve, left) and optically in units of photon counts per ms (red curve, right). The optical response curve is not linear, and defines a steep optimal working zone (dashed box). (d) A typical DNA translocation event (8 kbp) measured simultaneously electrically (blue, top) as well as optically (bottom, red) using the confocal mode ($V = 0.3$ V, 1 M KCl and 0.5 M $CaCl_2$ in *trans* side, data filtered at 10 kHz for display purpose; cps = counts per ms).

scheme of our confocal/TIRF apparatus is provided in the Supporting Information.

Finite-element modeling of the system with COMSOL (described below) shows that when the pore is electrically biased with a positive potential in the *trans* chamber, a steady flow of Ca^{2+} ions creates a steeply decreasing concentration gradient at the pore vicinity in the *cis* side. Moreover, the magnitude and characteristic size of the hemispherical Ca^{2+} ion gradient can be adjusted either statically (by setting the bulk $CaCl_2$ concentration in *trans*), chemically (by adjusting the concentration of a strong Ca^{2+} chelator, such as EGTA), or dynamically (by adjusting the *cis/trans* potential difference). Addition of Ca^{2+} indicator dye at low concentration to the *cis* side results in a highly localized and voltage-tunable fluorescent spot immediately outside the nanopore (Figure 1b). This phenomenon is shown in Figure 1c, where the fluorescence intensity (I_f , red trace) is measured at the pore location using the confocal setup as a function of the applied membrane voltage (V). At negative voltages, the fluorescence intensity is independent of voltage (no Ca^{2+} ions flow

from *trans* to *cis*), but when the voltage becomes positive we observe a sharp increase in the intensity of more than a factor of 10 in the range 0 to 1 V. The simultaneously measured ion current (I_i , blue trace) versus voltage V of this pore shows the typical asymmetric relationship with voltage due to the asymmetric electrolyte distribution across the pore. With positive voltage, the excess chloride ions in *trans* flow into the *cis*, whereas at negative voltage, the current is limited by the lower concentration of chloride ions in *cis* flowing into *trans*.

To demonstrate that the observed fluorescence intensity is a positive function of the magnitude of Ca^{2+} ions flowing through the pore (and not directly the applied voltage), we translocated dsDNA molecules (8 kbp) through the pore (from *cis* to *trans*), while simultaneously measuring I_f and I_i . Figure 1d shows a characteristic DNA translocation event measured at a constant voltage of 300 mV. The reduction in the ionic current is perfectly correlated with the reduction in the fluorescence intensity. Next we present a numerical model of the expected Ca^{2+} -dependent

signal, experimental characterization of I_f as compared to I_o , and simultaneous single-molecule measurements using I_f and I_o .

Theoretical Analysis Using Numerical Simulations. To simulate fluorescence intensity near the nanopore under our experimental conditions and pore geometry, we use Poisson–Nernst–Planck equations to model ionic concentration distributions near nanopores.^{38,39} We model the ionic current in 3D with a 2D axisymmetric simulation of a 4 nm pore in a 10 nm membrane surrounded by sphere of 1 μm radius of electrolyte solution where the pore is the only connection between the two chambers, as shown in Figure 2a (see details in the Supporting Information). The concentrations of calcium, potassium, and chloride are set at the *cis* and *trans* chamber boundaries, as is the electric potential for each simulation. The concentration of Ca^{2+} as a function of the vertical axis depth (z) centered at the pore, where calcium chloride concentration has been set to 1 M at the *trans* boundary and 0 at the *cis* boundary, is shown in Figure 2b for voltages from -1 to 1 V. It is apparent that the gradient of Ca^{2+} concentration near the pore is very sensitive to voltage, decaying on the order of a few nanometers to hundreds of nanometers within the range of experimental voltages. We note that this characteristic decay length can be made much smaller than the typical optical confocal length scale (a few hundreds of nm) or TIR evanescent wave (about 100 nm). Therefore, the spatial resolution of the optical sensing method is set by the chemical gradients near the pore and not by optics. The dependence of Ca^{2+} ion distributions as a function of the bulk concentration in *trans* is shown in Figure 2c, for *trans* bulk concentrations ranging from 10 mM to 3 M.

Next, we experimentally measured the apparent binding constants of dye– Ca^{2+} complexes for three different concentration of the chelator molecule (EGTA): 10, 50, and 100 mM (see Figure S2 in Supporting Information). The measured k_D values of 5.6, 20.5, and 34.2 mM were used to numerically calculate the spatial distribution of the dye– Ca^{2+} complexes by solving first order binding equations as shown in Figure 2d. In this calculation, we take advantage of the fact that in the pore vicinity (the “active zone”) Ca^{2+} concentration is always much larger than the dye concentration. While this calculation is approximate, it provides the important insight that the typical length scale over which the concentration of Ca^{2+} active dyes drops is substantially smaller than the “optical thickness” defined by either the TIRF field or the confocal volume (blue and green curves, respectively), and in fact can be further adjusted (by the EGTA, voltage and Ca^{2+} bulk concentration) to extend only a few nanometers away from the pore. Specifically, we approximate the characteristic decay distance, r_0 as the radius away from the pore where the dye– Ca^{2+} complexes concentration drops to 10% of its peak value. We

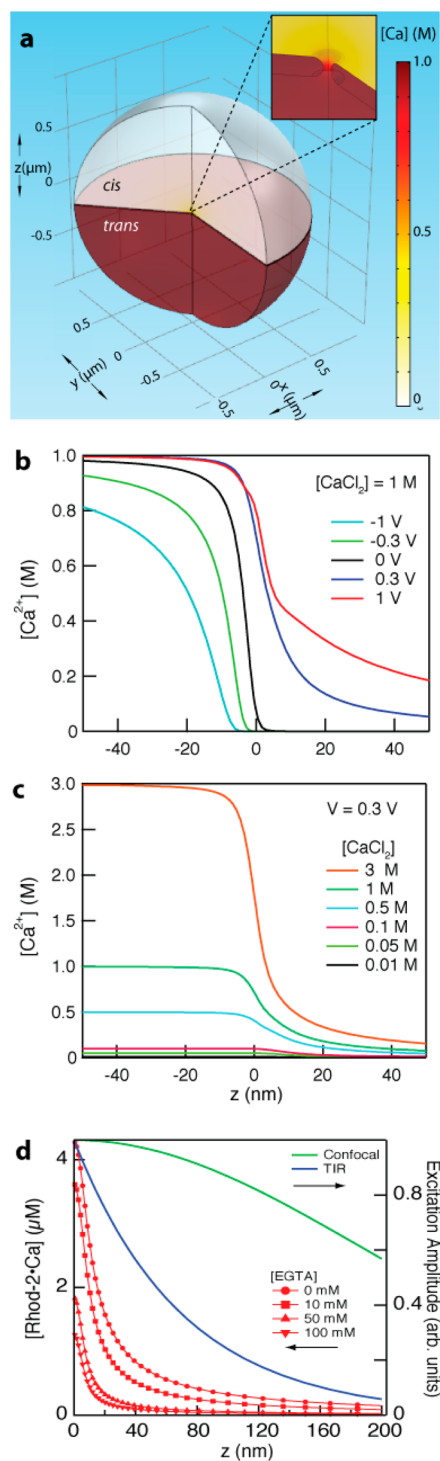


Figure 2. Numerical simulations of the steady-state ions spatial distribution near the nanopore. (a) Finite element 2D axisymmetric model of a nanopore surrounded by 1 μm of *cis* and *trans* chamber in all directions from the pore. (b and c) The space-dependent concentration of Ca^{2+} ions along the z -axis in the vicinity of the pore, as a function of applied voltage (b, bulk Ca^{2+} concentration in *trans* is 1 M) or as a function of Ca^{2+} concentration at a fixed applied voltage of 0.3 V (c). (d) The local concentration of the Ca^{2+} –Rhod-2 complex in the vicinity of the pore (for $z > 0$) as a function of EGTA, at fixed voltage and Ca^{2+} bulk concentration (0–100 and 10 mM, respectively) (red symbols and lines). The green and blue curves indicate the calculated normalized excitation amplitudes of the confocal and TIRF fields used in the experiments, respectively.

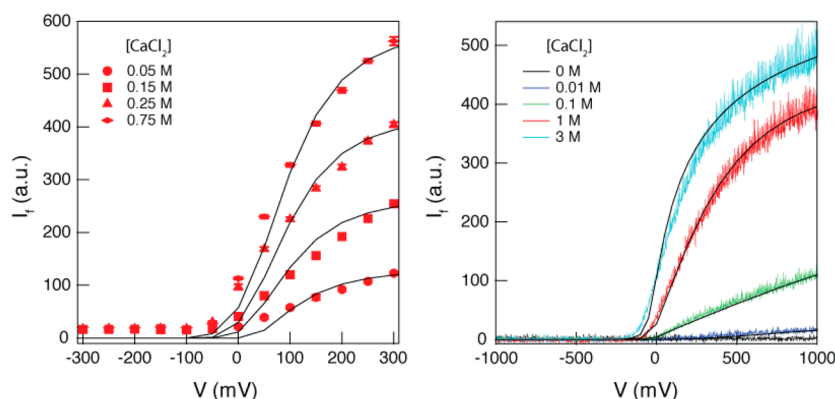


Figure 3. Validation of the numerical model with experimental measurements of the fluorescence intensity near a nanopore. The fluorescence intensity (I_f) was measured as a function of applied voltage using either the TIRF illumination (left panel) or the confocal illumination (right panel), for a stable open nanopore ($d = 4$ nm), at different bulk Ca^{2+} concentrations as indicated. In all cases, the fluorescence intensity was independent of voltages for negative voltages, and displayed a nonlinear saturating form for positive voltages. Black lines represent the corresponding fluorescence intensities calculated using the numerical model, as described in the text.

obtain $r_0 \approx 81, 60, 35, 31$ nm for $[\text{EGTA}] = 0, 10, 50, 100$ mM, respectively.

Validation of the Numerical Model. To validate our numerical model, we measured the fluorescence intensity under either TIRF imaging with $4 \mu\text{M}$ Fluo-4, or using confocal imaging with $5.7 \mu\text{M}$ Rhod-2 as a function of voltage (I_f – V curves), shown in Figure 3 left and right panels, respectively. These measurements were repeated at different *trans* bulk CaCl_2 concentrations, as indicated. We then compared the experimental results with our numerical prediction (normalized at 0.3 or 1 V for the TIRF and confocal data, respectively) shown as black lines in Figure 3. Despite the simplifications used in our model, our theoretical predictions of fluorescence strength fit well to our experimental results for both imaging modalities. At voltages above -100 mV, a fluorescence signal begins to rise above background levels sigmoidally as the Ca^{2+} reacts with Fluo-4 or Rhod-2 near k_D before proceeding into a linear phase, saturating the available indicator as $[\text{Ca}^{2+}] \gg [\text{Fluo-4}]$ or $[\text{Rhod-2}]$. Finally, the available indicator within the confocal observation volume or TIR evanescent field begins to saturate.

Optical versus Electrical Noise Spectra. To compare the electrical and optical noise characteristics, synchronous photon counts and ionic current were acquired for 5 s at 300 mV using a 4.5 nm pore (Figure 4a,b insets). This data was used to calculate the power spectra (Figure 4a, blue and Figure 4b, red) for the electrical and optical signals, respectively. The electrical spectrum displays the characteristic $1/f$ noise contribution (“flicker noise”) at low frequency and a $\sim f^2$ noise term above roughly 10 kHz, as well as some spurious electrical pickups and resonances (somewhat exaggerated due to openings in our Faraday box for the objective lens and stage controls). This shape and the various contributions across the frequency domain have been considered in the literature by multiple

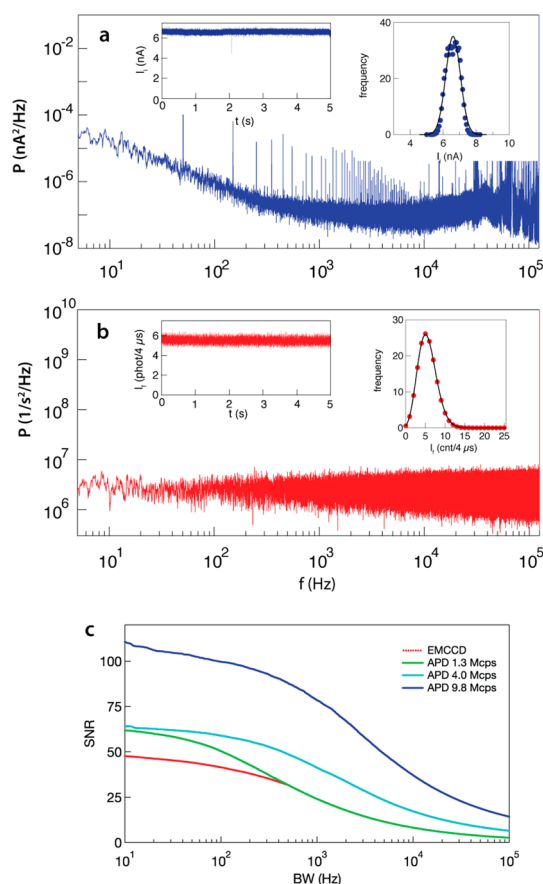


Figure 4. Electrical and optical noise spectra. The electrical noise (a) exhibits low frequencies “flicker” noise characteristic to the nanopore system, as well as $\sim f^2$ growing noise amplitude (“capacitance noise”), on top of the fundamental Johnson noise. (Inset) The electrical current histogram fit with a Gaussian distribution (mean = 6.57 ± 0.03 nA, width = 0.77 ± 0.07 , $\chi^2 = 2.25$) shows deviations at the peak and tails. Optical noise (b) is spectrally flat. (Inset) Optical noise shows a near perfect fit to a Poisson distribution (mean = 5.55 ± 0.01 cnts/ $4 \mu\text{s}$, $\chi^2 = 0.96$). The signal to noise ratios (SNR) for the optical signals (c) were evaluated as a function of the measurement bandwidth, as explained in the text, showing positive function of the total number of counts.

groups.^{25–27,40} In contrast, the corresponding optical spectrum is virtually flat from 5 to 10⁵ Hz, and specifically no spurious noise is observed. We further analyzed our signals by fitting the raw data as shown in Figure 4a,b, right insets. An ideal ion current signal would result in a perfectly normal distribution; however, careful analysis shows significant deviation from a single Gaussian (black curve) for the electrical signal at the peak of the function, where the Gaussian fit overestimates the data. We note that this deviation is the direct consequence of the shape of the electrical noise spectra shown in Figure 4a, specifically caused by the 1/*f* flicker noise. Since fluctuations in the signal mean are used to detect translocation events, these deviations directly reduce the quality of the electrical signal for translocation detection. In contrast, the optical signal, *measured synchronously with the electrical current*, is very well modeled by a Poisson distribution (black curve), a strong indication that the optical signal exhibits shot noise only.

We further evaluated the signal-to-noise ratio (SNR) of the optical signals as a function of the mean fluorescence intensities. Following the definition of SNR presented in Ivankin *et al.*³⁷ ($\text{SNR} = I_{\text{avg}}/I_{\text{RMS}}(\text{BW})$) where I_{avg} is the average intensity and $I_{\text{RMS}}(\text{BW}) = (\int^{\text{BW}} \text{PSD } d\eta)^{1/2}$ we show the SNR for TIRF with an EMCCD as well as confocal APD counts for three fluorescence intensities (1.3, 4.0, and 9.8 Mcps) in Figure 4c. The SNR is shown to be a positive function of the total number of counts, which may be tuned *via* the activated fluorophore concentration and excitation intensity.

We argue that the observed difference in noise profile for simultaneously acquired optical and electrical ion current signals is a consequence of two fundamental properties of the optical measurements: First, as demonstrated by the numerical simulation, the photon flux is generated in the immediate vicinity of the nanopore aperture due to the strong gradient of Ca²⁺ ion concentration. In contrast, the electrical ion current, measured at the electrodes hundreds of micrometers from the nanopore, involves both local and nonlocal fluctuations in potential and currents (*e.g.*, parasitic capacitances in the SiN_x membrane contribute to the pore noise). Second, photon arrivals are an inherently digital stream of information, whereas the electrical ion current is an analog signal, subject to sampling error and noise. Additionally, the optical signal does not suffer from electromagnetic pick-up or ground loops known to deteriorate low-noise electrical recordings. Indeed, the discrete noise pickup frequencies in the electrical power spectrum in Figure 4a are clearly absent from the optical power spectrum in Figure 4b.

Synchronous Optical and Electrical Single-Molecule Detection.

We compare electrical and optical nanopore sensing methods by recording sets of DNA translocations

synchronously. Figure 5a displays a typical set of DNA translocations (8 kbp) through a 4 nm pore recorded using confocal mode ($V = 300$ mV, 285 μM Rhod-2 in *cis* and 500 mM CaCl₂ in *trans* in addition to 1 M KCl in both chambers). The top panel displays the electrical ion current traces (blue) and the bottom panel displays the optical events (red). Synchronous recording of the electrical and optical signals was ensured by sharing the same clock and start trigger pulses for the two acquisition cards, and data was analyzed by extracting the exact same temporal sections from the data files. Figure 5a clearly shows that the optical data mirrors the electrical data. Synchronous recordings of additional DNA lengths (1, 8, and 10 kbp) using TIRF are shown in the Supporting Information Figure S9.

We further analyzed ~150 translocation events using both the confocal and TIRF modes. Each event was analyzed independently to extract its dwell time (t_D) and event amplitude (ΔI) both on the electrical and the optical data traces. Figure 5b shows that t_D values extracted optically as compared to electrically are essentially identical. In contrast, the event amplitude values, measured optically as compared to electrically, yield a more complicated trend: while generally there is a clear linear correlation between electric and optical event amplitudes, we observe a wider spread of values between the two measurements types. Referring back to Figure 1c, we note that the optical signal exhibits a steeper and nonlinear dependence on the voltage, and hence on the pore conductance, which is dominated by K⁺ and Cl[−] ion flow. Specifically, the large slope of the optical response curve in Figure 1c may amplify small fluctuations in pore conductance, resulting in a larger spread in ΔI as compared with ΔI_e . Additionally, we cannot rule out other possible mechanisms, such as specific Ca²⁺ divalent ion binding to the translocating DNA molecules, which would affect the optical signal more than the electrical one. Approximating the pore as a 10 nm cylinder 4 nm in diameter with 50 mM Ca²⁺, there will on average only be ~4 Ca²⁺ ions within the pore at a time relative to ~30 nucleotide base-pairs of translocating DNA. Given that DNA binds calcium ions,⁴¹ it is reasonable that Ca²⁺ blockades may differ from K⁺ or Cl[−] blockades. These mechanisms will be the subject of further study. We also note that having an asymmetric distribution of ions in the nanopore setup increased the capture rate (Supporting Information Figure S6) while simultaneously slowing down each translocation, similar to previous reports for monovalent asymmetric salt conditions.³⁸

Parallel Optical Detection with Solid-State Nanopore Arrays.

An additional prominent advantage of optical detection over electrical detection is the ability to optically address multiple nanopores without requiring complex fabrication of individual sets of electrodes (along with the electrical isolation of each channel) for each pore. This feature is crucial for applications requiring

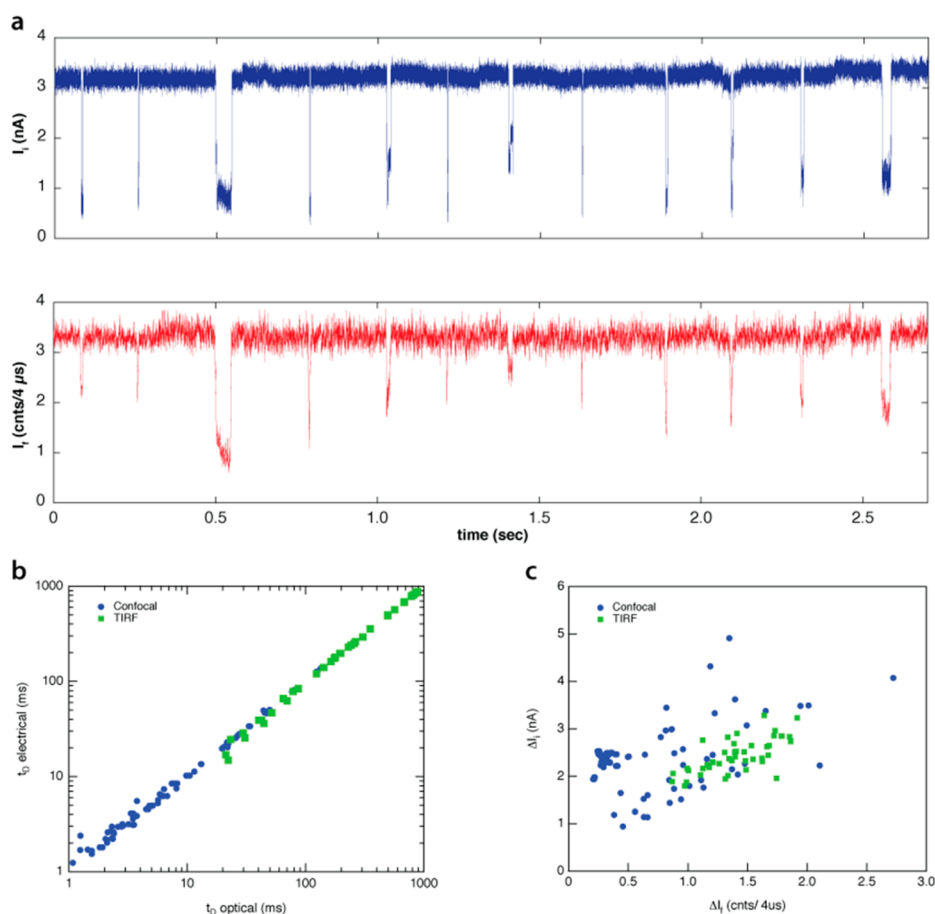


Figure 5. Simultaneous electrical and optical recording of DNA translocations through solid-state nanopores. (a) Concatenated typical traces of DNA translocation events recorded using the confocal mode ($d = 4.5$ nm, $V = 0.3$ V, 1 M KCl and 0.5 M CaCl_2 in *trans* side). Electrical ion current shown in blue (top panel) and optical signals in red (bottom panel). The delay time between events was removed for clarity. (b) A comparison of event dwell times, probed either electrically or optically, using the confocal or TIRF modes (blue and green, respectively). Optical and electrical dwell times are essentially identical. (c) Event amplitudes measured for the electrical and optical traces (as shown in a).

massive parallelization, such as high-throughput sequencing. To demonstrate the feasibility of parallel optical detection we fabricated a 3-by-3 nanopore array using a TEM ($d = 4.0 \pm 1.0$ nm, pitch = 5 μm , see Figure 6b). With 20 μM Fluo-4 in *cis* at 300 mV under 488 nm illumination, each pore fluoresces as shown in Figure 6a. The total ionic current recorded from the nine pores is essentially an ensemble measurement and provides very little information. With optical measurements, we can decouple these individually and detect which pores are open and translocating, which are partially opened, and which are partially blocked. This is illustrated with a set of continuous simultaneous recordings (30 s long) from these nine nanopores, shown in Figure 6c. Out of the nine nanopores probed simultaneously in this measurement four displayed DNA translocation events (8 kbp), one became partially blocked after 20 s, and the other pores remained open. Some fluctuation in the baseline optical signal was observed over the course of this experiment, which may have arisen due to slow drift of the membrane relative to the objective over the

course of a long (30 s) continuous movie and/or from optical cross-talk between pores (*i.e.*, a nearby pore's fluorescence intensity shows up weakly in neighboring pores, depending on pitch, the amplitude of the fluctuation, and the fluorescence spot size).

CONCLUSION

In this report, we have described an improved method for purely optical single-molecule detection of unlabeled analytes passing through solid-state nanopores. Our main motivation for supplementing or substituting electrical readout with optical readout, illustrated by numerical simulations, was that sharp Ca^{2+} ion gradients can be established in the close vicinity to the nanopore aperture with a spatial decay of just a few nanometers (Figure 2b,c). Coupled with Ca^{2+} indicator dyes, this phenomenon can be utilized to optically probe the local ion current flow in the pore with high spatiotemporal resolution. Unlike the electrical ion current signal that is broadly used in the nanopore field, the optical approach is virtually immune to spurious EM noise pick-up or parasitic capacitance

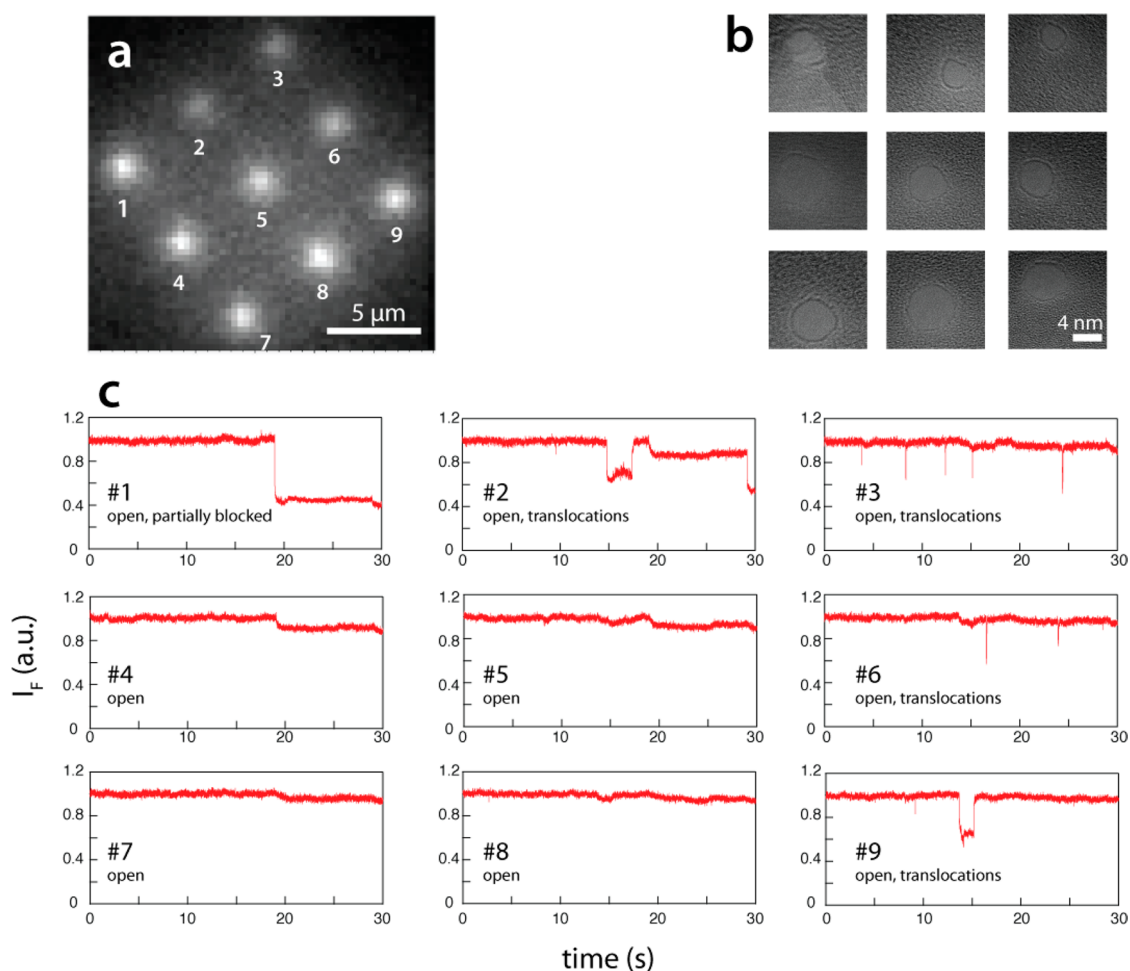


Figure 6. (a) Image of 3×3 array of pores with $20 \mu\text{M}$ Fluo-4 in *cis* chamber at 50 mM CaCl_2 in *trans* at 300 mV in TIRF microscope. (b) HR-TEM images of 9 $4 \pm 1 \text{ nm}$ pores drilled in a 3×3 array. (c) Fluorescence modulations associated with 8 kbp DNA at 500 mV for each of the nine pores.

noise sources, and hence exhibits a superior spectral response (Figure 4b). We experimentally demonstrated this effect by simultaneous electrical and optical recordings of DNA translocations passing through both single nanopores and nanopore arrays.

An advantage of ion current based probing in nanopores as compared to optical sensing is the higher baseline level of the electrical signal: A typical 1 nA current in solid-state nanopore corresponds to a flux of $\sim 6 \times 10^9 \text{ e/s}$, while the highest photon flux reported in this study is roughly 2 orders of magnitude smaller ($\sim 10^7$ photons/s). This clearly translates to a superior SNR for electrical measurements when calculated similarly to Figure 5. However, this advantage comes at the expense of using nonphysiological high salt concentrations (typically 1 M monovalent salt) and a nonideal power spectrum. Moreover, our numerical simulations show that the concentration of the Ca^{2+} bounded dyes decays nearly exponentially away from the pore, with characteristic length scale of $r_0 \sim 81 \text{ nm}$. This distance will set the upper limit on the temporal response time of the optical sensing method, associated with the diffusion time of the dyes, which can be

estimated by $t_D = r_0^2/6D$, where $D \sim 400 \mu\text{m}^2/\text{s}$ is the dye's diffusion constant. Setting $r_0 = 81 \text{ nm}$, we obtain $t_D \sim 3.0 \mu\text{s}$. Furthermore, taking into account the binding kinetics of the dye and the competition with the Ca^{2+} chelator EGTA, we showed in Figure 2d that the characteristic distance can be further reduced. For example at 100 mM EGTA, $r_0 \sim 31 \text{ nm}$ producing even faster theoretical response time of $\sim 0.4 \mu\text{s}$.

Advances in single-molecule fluorescence methods are likely to offer further improvements to optical sensing, with the introduction of local light-enhancement structures, lower optical background materials and higher-brightness fluorophores. Notably, in our method each Ca^{2+} ion traversing through the pore and activating a single fluorophore molecule could emit a *burst* of multiple photons prior to chelation, while it is located within nanometers of the pore. This effective amplification of the signal provides a fundamental advantage over direct electrical ion measurements. It strictly requires the utilization of sufficiently strong excitation and emission count rates, which to the best of our knowledge have never been coupled to a nanopore system. This regime will potentially allow researchers to obtain

even higher bandwidth than state-of-the-art electrical sensing, and will be directly applicable to nanopore-

based DNA sequencing and epigenetic analyses, which will be the subject of future work.

METHODS

Chip and Nanopore Fabrication. Nanopore chips were fabricated on a 4 in. silicon wafer coated with SiO₂ (500 nm) and low-stress amorphous silicon nitride (SiN_x, 60 nm). The SiN_x was locally thinned to 10 nm (1.5–2 μ m circular wells) using a controlled RIE etch. Freestanding membranes of SiN_x (60 \times 60 μ m) were created by through-etching the wafer with KOH, with the locally etched wells aligned to the etched freestanding SiN_x membranes. Nanopores were fabricated in the thinned SiN_x regions using a high resolution aberration-corrected TEM (Titan 80–300 FEG-S/TEM, FEI) or a noncorrected TEM (JEOL 2010F), as previously reported.⁴² Pore formation proceeded with visual feedback by iterating through a uniformly expanded beam for imaging the nanopore diameter during formation and converging the beam to locally sputter and melt the membrane. Pores of 4 \pm 0.2 nm could be consistently formed. NoLimits dsDNA (One kbp, 8, and 10 kbp) was purchased from Fisher Scientific (SM1671, SM1521, and SM1751, respectively). Tripotassium Rhod-2 (F-142200) and pentapotassium Fluo-4 (F-14200) salts were purchased from Life Technologies and stored in 15 mM 5 μ L aliquots in Milli-Q water at –20 °C until use.

Electro-Optical Measurement System. Chips with nanopores were boiled in piranha solution (1:3 concentrated sulfuric acid/30% (w/v) H₂O₂) at 120 °C for 15 min prior to use in experiments.⁴³ The chips were then thoroughly rinsed in Milli-Q water (EMD Millipore), vacuum-dried, and mounted in custom CTFE cells with Ecoflex 5 (Smooth-ON) silicone rubber to separate *cis* from *trans* sides of the membrane, before rewetting in 1 M KCl buffered to pH 7.2 with HEPES or Tris-EDTA with 10 mM EGTA and either Rhod-2 or Fluo-4 (5–270 μ M) added to the *cis* chamber and calcium chloride (CaCl₂, 10–500 mM) added to the *trans* chamber (concentrations varied by experiment). Ag/AgCl electrodes were immersed in *cis* and *trans* and connected to an Axopatch 200B (Molecular Devices). A positive electric bias corresponds to the cathode in the *cis* and the anode in the *trans*, electrophoretically driving Ca²⁺ from *trans* to *cis* and DNA from *cis* to *trans*.

The nanochip was mounted on a closed-loop XYZ nanopositioner (Physik Instrumente, P-561.3CD) on top of a high-NA objective (Olympus Plan Apochromat 60 \times /1.45) in a custom microscope (Supporting Information Figure S10). For excitation, we used one of two solid-state lasers: 488 nm (Coherent Sapphire), or 532 nm (QIOptiq, iFlex Mustang), coupled by single mode, polarization-preserving optical fibers. The laser beams were attenuated using a half wavelength plate and expanded using a custom telescope that could be configured for both confocal illumination (collimated beam output) or a converging beam at the objective back focal plane.³⁰ Emitted light was collected by the same objective and was filtered using the appropriate notch filters (Semrock) and then focused using a single 20 cm focal length lens onto either an EM-CCD camera (Andor iXon 897) in the TIRF mode or to a 25 μ m pinhole (Thorlabs) in the confocal mode. Light passing through the pinhole was collimated using a 10 cm lens, split at $L = 640$ nm using a dichroic mirror (Semrock) and focused using two additional 2.5 cm focal distance lenses onto two APD's (Perkin Elmer SPCM-AQR-14). All lenses were obtained from Thorlabs. For data acquisition, we used National Instruments NI-6534 DAQs for analog signals and NI-6602 for photon counting. The two cards shared the same 250 kHz sampling clock via a hardware connection, and were fully controlled by a custom LabView (National Instrument) program, that was also used to control the EM-CCD and acquire movies. Synchronization with the camera was achieved by connecting the iXon's fire signal to an additional counter, thus providing exact timing of each camera frame.³⁰

Conflict of Interest: The authors declare no competing financial interest.

Supporting Information Available: Scheme of experimental setup; Rhod-2-Ca²⁺ binding constant measurements for different EGTA concentrations; fluorescence intensity *versus* voltage curves at different CaCl₂ and EGTA concentrations; numerical model of Ca²⁺-bound dye concentration distributions near a solid-state nanopore; asymmetric *trans/cis* calcium concentration increases capture rate and slows translocation; synchronous electrical and optical translocation blockade depth. This material is available free of charge via the Internet at <http://pubs.acs.org>.

Acknowledgment. We acknowledge financial support from the National Institutes of Health (NHGRI Grant No. R01 HG-005871), from the Marie Curie People award (GA-2010- 277060, ERC) and from the Israeli Centers of Research Excellence (I-CORE) programme (Center #1902/12). The authors also thank the staff at the Harvard University Center for Nanoscale Sciences (CNS) and the Technion Electron Microscopy Center for dedicated support. B.N.A. was responsible for nanopore fabrication, designing and performing experiments, analyzing data, and manuscript writing. O.N.A. performed experiments and analyzed data. T.G. performed experiments and analyzed data. A.H.S. performed nanopore fabrication and write manuscript. D.B. performed nanopore fabrication. A.M. designed experiments, set up construction, analyzed data, wrote manuscript.

REFERENCES AND NOTES

- Venkatesan, B. M.; Bashir, R. Nanopore Sensors for Nucleic Acid Analysis. *Nat. Nanotechnol.* **2011**, *6*, 615–624.
- Wanunu, M. Nanopores: A Journey towards DNA Sequencing. *Phys. Life Rev.* **2012**, *9*, 125–158.
- Kasianowicz, J. J.; Brandin, E.; Branton, D.; Deamer, D. W. Characterization of Individual Polynucleotide Molecules Using a Membrane Channel. *Proc. Natl. Acad. Sci. U.S.A.* **1996**, *93*, 13770–13773.
- Meller, A.; Nivon, L.; Brandin, E.; Golovchenko, J.; Branton, D. Rapid Nanopore Discrimination between Single Polynucleotide Molecules. *Proc. Natl. Acad. Sci. U.S.A.* **2000**, *97*, 1079–1084.
- Akeson, M.; Branton, D.; Kasianowicz, J. J.; Brandin, E.; Deamer, D. W. Microsecond Time-Scale Discrimination among Polycytidylic Acid, Polyadenylic Acid, and Polyuridylic Acid as Homopolymers or as Segments within Single RNA Molecules. *Biophys. J.* **1999**, *77*, 3227–3233.
- Firnkies, M.; Pedone, D.; Knezevic, J.; Döblinger, M.; Rant, U. Electrically Facilitated Translocations of Proteins through Silicon Nitride Nanopores: Conjoint and Competitive Action of Diffusion, Electrophoresis, and Electroosmosis. *Nano Lett.* **2010**, *10*, 2162–2167.
- Yusko, E. C.; Johnson, J. M.; Majd, S.; Prangko, P.; Rollings, R. C.; Li, J.; Yang, J.; Mayer, M. Controlling Protein Translocation through Nanopores with Bio-Inspired Fluid Walls. *Nat. Nanotechnol.* **2011**, *6*, 253–260.
- Larkin, J.; Henley, R. Y.; Muthukumar, M.; Rosenstein, J. K.; Wanunu, M. High-Bandwidth Protein Analysis Using Solid-State Nanopores. *Biophys. J.* **2014**, *106*, 696–704.
- Stoloff, D. H.; Wanunu, M. Recent Trends in Nanopores for Biotechnology. *Curr. Opin. Biotechnol.* **2013**, *24*, 699–704.
- Manrao, E. A.; Derrington, I. M.; Laszlo, A. H.; Langford, K. W.; Hopper, M. K.; Gillgren, N.; Pavlenok, M.; Niederweis, M.; Gundlach, J. H. Reading DNA at Single-Nucleotide Resolution with a Mutant MspA Nanopore and Phi29 DNA Polymerase. *Nat. Biotechnol.* **2012**, *30*, 349–353.
- Cherf, G. M.; Lieberman, K. R.; Rashid, H.; Lam, C. E.; Karplus, K.; Akeson, M. Automated Forward and Reverse Ratcheting of DNA in a Nanopore at 5-A Precision. *Nat. Biotechnol.* **2012**, *30*, 344–348.

12. Clarke, J.; Wu, H. C.; Jayasinghe, L.; Patel, A.; Reid, S.; Bayley, H. Continuous Base Identification for Single-Molecule Nanopore DNA Sequencing. *Nat. Nanotechnol.* **2009**, *4*, 265–270.
13. Ayub, M.; Hardwick, S. W.; Luisi, B. F.; Bayley, H. Nanopore-Based Identification of Individual Nucleotides for Direct Rna Sequencing. *Nano Lett.* **2013**, *13*, 6144–6150.
14. Shasha, C.; Henley, R. Y.; Stoloff, D. H.; Rynearson, K. D.; Hermann, T.; Wanunu, M. Nanopore-Based Conformational Analysis of a Viral Rna Drug Target. *ACS Nano* **2014**, *8*, 6425–6430.
15. Cracknell, J. A.; Japrun, D.; Bayley, H. Translocating Kilo-base Rna through the Staphylococcal Alpha-Hemolysin Nanopore. *Nano Lett.* **2013**, *13*, 2500–2505.
16. Ayub, M.; Bayley, H. Individual Rna Base Recognition in Immobilized Oligonucleotides Using a Protein Nanopore. *Nano Lett.* **2012**, *12*, 5637–5643.
17. Singer, A.; Rapireddy, S.; Ly, D. H.; Meller, A. Electronic Barcoding of a Viral Gene at the Single-Molecule Level. *Nano Lett.* **2012**, *12*, 1722–1728.
18. Fologea, D.; Uplinger, J.; Thomas, B.; McNabb, D. S.; Li, J. Slowing DNA Translocation in a Solid-State Nanopore. *Nano Lett.* **2005**, *5*, 1734–1737.
19. Kowalczyk, S. W.; Wells, D. B.; Aksimentiev, A.; Dekker, C. Slowing Down DNA Translocation through a Nanopore in Lithium Chloride. *Nano Lett.* **2012**, *12*, 1038–1044.
20. Di Fiori, N.; Squires, A.; Bar, D.; Gilboa, T.; Moustakas, T. D.; Meller, A. Optoelectronic Control of Surface Charge and Translocation Dynamics in Solid-State Nanopores. *Nat. Nanotechnol.* **2013**, *8*, 946–951.
21. Anderson, B. N.; Muthukumar, M.; Meller, A. pH Tuning of DNA Translocation Time through Organically Functionalized Nanopores. *ACS Nano* **2013**, *7*, 1408–1414.
22. Squires, A. H.; Hersey, J. S.; Grinstaff, M. W.; Meller, A. A Nanopore-Nanofiber Mesh Biosensor to Control DNA Translocation. *J. Am. Chem. Soc.* **2013**, *135*, 16304–16307.
23. Rosenstein, J. K.; Wanunu, M.; Merchant, C. A.; Drndic, M.; Shepard, K. L. Integrated Nanopore Sensing Platform with Sub-Microsecond Temporal Resolution. *Nat. Meth.* **2012**, *9*, 487–U112.
24. Tabard-Cossa, V.; Trivedi, D.; Wiggin, M.; Jetha, N. N.; Marziali, A. Noise Analysis and Reduction in Solid-State Nanopores. *Nanotechnology* **2007**, *18*, 305505.
25. Smeets, R.; Keyser, U.; Dekker, N. H.; Dekker, C. Noise in Solid-State Nanopores. *Proc. Natl. Acad. Sci. U.S.A.* **2008**, *105*, 417–421.
26. Hoogerheide, D. P.; Garaj, S.; Golovchenko, J. A. Probing Surface Charge Fluctuations with Solid-State Nanopores. *Phys. Rev. Lett.* **2009**, *102*, 256804.
27. Smeets, R.; Dekker, N.; Dekker, C. Low-Frequency Noise in Solid-State Nanopores. *Nanotechnology* **2009**, *20*, 095501.
28. McNally, B.; Singer, A.; Yu, Z.; Sun, Y.; Weng, Z.; Meller, A. Optical Recognition of Converted DNA Nucleotides for Single-Molecule DNA Sequencing Using Nanopore Arrays. *Nano Lett.* **2010**, *10*, 2237–2244.
29. Chansin, G. A.; Mulero, R.; Hong, J.; Kim, M. J.; DeMello, A. J.; Edel, J. B. Single-Molecule Spectroscopy Using Nanoporous Membranes. *Nano Lett.* **2007**, *7*, 2901–2906.
30. Soni, G. V.; Singer, A.; Yu, Z.; Sun, Y.; McNally, B.; Meller, A. Synchronous Optical and Electrical Detection of Biomolecules Traversing through Solid-State Nanopores. *Rev. Sci. Instrum.* **2010**, *81*, 014301.
31. Singer, A.; McNally, B.; Torre, R. D.; Meller, A. DNA Sequencing by Nanopore-Induced Photon Emission. *Methods Mol. Biol.* **2012**, *870*, 99–114.
32. Ando, G.; Hyun, C.; Li, J.; Mitsui, T. Directly Observing the Motion of DNA Molecules near Solid-State Nanopores. *ACS Nano* **2012**, *6*, 10090–10097.
33. Kurz, V.; Nelson, E. M.; Shim, J.; Timp, G. Direct Visualization of Single-Molecule Translocations through Synthetic Nanopores Comparable in Size to a Molecule. *ACS Nano* **2013**, *7*, 4057–4069.
34. Auger, T.; Mathe, J.; Viasnoff, V.; Charron, G.; Di Meglio, J. M.; Auvray, L.; Montel, F. Zero-Mode Waveguide Detection of Flow-Driven DNA Translocation through Nanopores. *Phys. Rev. Lett.* **2014**, *113*, 028302.
35. Heron, A. J.; Thompson, J. R.; Cronin, B.; Bayley, H.; Wallace, M. I. Simultaneous Measurement of Ionic Current and Fluorescence from Single Protein Pores. *J. Am. Chem. Soc.* **2009**, *131*, 1652–1653.
36. Anderson, B. N. Enhancing the Temporal and Spatial Resolution of Solid-State Nanopore Single-Molecule Sensors. Ph.D. Dissertation, Boston University, Boston, MA, 2013.
37. Ivankin, A.; Henley, R. Y.; Larkin, J.; Carson, S.; Toscano, M. L.; Wanunu, M. Label-Free Optical Detection of Biomolecular Translocation through Nanopore Arrays. *ACS Nano* **2014**, *8*, 10774–10781.
38. Wanunu, M.; Morrison, W.; Rabin, Y.; Grosberg, A. Y.; Meller, A. Electrostatic Focusing of Unlabelled DNA into Nanoscale Pores Using a Salt Gradient. *Nat. Nanotechnol.* **2010**, *5*, 160–165.
39. Powell, M. R.; Sullivan, M.; Vlassioulis, I.; Constantin, D.; Sudre, O.; Martens, C. C.; Eisenberg, R. S.; Siwy, Z. S. Nanoprecipitation-Assisted Ion Current Oscillations. *Nat. Nanotechnol.* **2008**, *3*, 51–57.
40. Uram, J. D.; Ke, K.; Mayer, M. Noise and Bandwidth of Current Recordings from Submicrometer Pores and Nanopores. *ACS Nano* **2008**, *2*, 857–872.
41. Dobi, A.; v Agoston, D. Submillimolar Levels of Calcium Regulates DNA Structure at the Dinucleotide Repeat (Tg/Ac)N. *Proc. Natl. Acad. Sci. U.S.A.* **1998**, *95*, 5981–5986.
42. Kim, M. J.; Wanunu, M.; Bell, D. C.; Meller, A. Rapid Fabrication of Uniformly Sized Nanopores and Nanopore Arrays for Parallel DNA Analysis. *Adv. Mater.* **2006**, *18*, 3149–3153.
43. Wanunu, M.; Meller, A. Chemically Modified Solid-State Nanopores. *Nano Lett.* **2007**, *7*, 1580–1585.